Visual and Near-Infrared Photometric Observations of Betelgeuse

Rick Wasatonic

Department of Astrophysics and Planetary Science, Villanova University, Villanova, PA 19085; richard.wasatonic@villanova.edu

Abstract   From 1996 to 2021 time-series photoelectric photometry of the M1-M2Ia-Iab red supergiant Betelgeuse was conducted using a wide-band V-filter centered on $\lambda555$ nm and narrow to intermediate-band Wing near infrared (NIR) titanium oxide (TiO) filters centered on $\lambda719$ nm, $\lambda754$ nm, and $\lambda1024$ nm. The observations were made to continually monitor magnitude variations for periodicities and variable amplitudes, calculate seasonal changes of effective temperatures, size, and luminosities, and subsequently examine the interrelationships among these physical properties. Using the V-band observations, short- and long-term dominant periods of 439 ± 5 and 2209 ± 183 days, respectively, were found. Effective temperatures varied from 3528 K to 3731 K, and using an adopted distance of 197 PC, luminosities varied from $70564\,L_{\odot}$ to $114204\,L_{\odot}$. Using these estimated values of effective temperature and luminosity, calculated radii, assuming spherical symmetry, varied from $710\,R_{\odot}$ to $847\,R_{\odot}$. NIR to V-band flux ratios indicate that Betelgeuse radiates, on the average, ~10 to ~20 times more in the NIR bands than the visual band. After NIR magnitude conversions from $\lambda1024$ nm to $\lambda1040$ nm, a surprising result was that the $\lambda754$-nm/$\lambda1040$-nm flux ratio was nearly 1.0, indicating the bolometric magnitude can be approximated at the shorter wavelength ($\lambda754$ nm) magnitude in addition to the theoretically-thought longer ($\lambda1040$ nm) wavelength magnitude.

1. Introduction

Betelgeuse (HD 39801, HR 6201) is one of the best known and most observed stars. It is a bright (nominal V ~0.3 to V ~0.9) semiregular pulsating red (B–V~1.85) supergiant of spectral type M1-M2Ia-Iab, belonging to the Orion OB1 association (Kaler 2001). Petit (1987) classifies it as an SRc variable; these stars are all extremely bright M-type supergiants with semiregular periods and variable amplitudes. The unpredictable nature of the star became most apparent during the 2019/2020 observing season when its V-band magnitude dropped to an unprecedented value of V~1.6 at minimum; this unusual occurrence became known as the Great Dimming Event (GDE). This relatively deep minimum occurred after 23 years of prior observations recorded some seasonal minima only near V = ~0.9. The GDE was noticed by both professional and amateur astronomical alike (e.g. Guinan *et al.* 2019a, 2019b) with various theoretical explanations such as reinforcement of multi-periodic minima occurring simultaneously (Guinan *et al.* 2019b) or the development of a dust cloud formed by condensing hot chromospheric material (Dupree *et al.* 2020). Related to this current study, there are many literature references that describe specific aspects of the variability nature of the star; Dupree *et al.* (1987) describe both photometric and spectroscopic variations from which a periodicity of 1.15 years (420 days) was detected; O'Gorman *et al.* (2015) report size and temperature relationships in the outer atmosphere of the star with the mean gas temperature dropping from 3000 K at $2R_{\star}$ to 1800 K at $6R_{\star}$. O'Gorman *et al.* also adopt a photospheric angular diameter of 42.45 milliarcseconds (mas), which, using Harper *et al.*'s (2008) estimated distance of 197 PC, reveals an actual photospheric size of $886\,R_{\odot}$. Townes *et al.* (2009) also report on a continual decrease in the size of Betelgeuse from 57 mas to 48 mas over 15 years using infrared spatial interferometric techniques at $\lambda11.15$ μm; again, using the estimated distance of 197 PC the change in size would be from $1190\,R_{\odot}$ to $1002\,R_{\odot}$, further implying that estimates of the linear size are dependent on the wavelength used to conduct the observations. However, despite its relative proximity to Earth, apparent brightness, and large size, there are significant degrees of uncertainties regarding the measures of its physical properties and other parameters such as distance and periodicities.

Dolan *et al.* (2016) neatly summarize a wealth of data on Betelgeuse from prior observations and analyses. This information is given in Tables 1, 2, and 3 of that paper, which includes various distance and radial velocity estimates, estimates of variable V-band magnitudes, luminosities, effective temperatures, and angular diameters that are again wavelength-dependent. Table 1 lists the adopted values of Dolan *et al.*'s V-band magnitude, $L/L_{\odot}$, T_{eff}, and $R/R_{\odot}$ averages; it will be seen in the following sub-sections and further subsequent papers that the photometric observations and resultant calculated parameters compare well with Dolan *et al.*'s adopted values.

Note that Dolan *et al.*'s adopted value of $887\,R_{\odot}$ was calculated by using the estimation of 197 PC as the distance to Betelgeuse (Harper *et al.* 2008) and an adopted value of 41.9 ± 0.06 mas based on Perrin *et al.*'s (2004) uniform disk diameter corrections.

2. Instrumentation and calibrations

The photoelectric observations were conducted using f/10 20-cm (8-inch) and f/10 27.5-cm (11-inch) Schmidt-Cassegrain telescopes at the Wasatonic Observatory near Allentown, Pennsylvania. An uncooled Optec SSP-3 photometer was

Table 1. Betelgeuse values adopted from Dolan (2016).

Parameter	Adopted Value
V-band (Å 555 nm)	0.51 mag
T_{eff}(K)	3500 ± 200
Log $(L_{\star}/L_{\odot})$	5.10
$R_{\star}/R_{\odot}$	887 ± 203

Table 2. Characteristics of the four wavelength-band filters.

Filter	Spectral Region	Central Wavelength (nm)	Bandpass (nm-FWHM)
V	—	555	240
A	TiO (δ; 0,0)	719	11
B	continuum	754	11
C	continuum	1024	42

mated to the telescopes; the SSP-3 has a silicon red-sensitive PIN-photodiode detector that has a broad spectral range from $\lambda 300$ nm to $\lambda 1100$ nm. The detector aperture size was 1.0 mm, which converts to a FOV aperture angular size of 74 arcseconds. Integration times for accumulating raw photometer counts were generally 30 to 50 seconds, depending on the variations of the counts themselves. Four-filter photometry was conducted; specific characteristics of the four filters are given in Table 2, where the features for the near-IR filters are adapted from Wing (1992).

The Wing A-band filter measures the TiO $\lambda 719$-nm $(\delta; 0,0)$ band, while the central wavelengths of the B- and C-band filters are located in NIR continuum regions that are relatively free from strong absorption lines. A molecular TiO index was calculated from the reduced Wing A-, B- and C-filter magnitudes via Equation 1 below, which is adopted from Wing (1992):

$$\text{TiO Index} = A - B - [0.13 \star (B - C)] \qquad (1)$$

The TiO index variations occur because the strengths of the TiO bands respond to changes in temperature (Wasatonic *et al.* 2015). Coupled with suitable TiO/effective temperature calibrations using known standard stars, changing effective temperatures can then be estimated as the TiO indices vary.

The spectral features of M-giants and supergiants display increasing strengths of TiO molecular lines as the effective temperature decreases and as the spectral sub-types progress from M0 to M8. The TiO/T_{eff} and TiO/M-Spectral Type calibrations that were used to compute the changing effective temperatures and spectral types are given in Equations 2a and 2b and are graphically displayed in the upper and lower panels of Figure 1, respectively.

$$T_{eff}(K) = 63.931 * (\text{TiO Index})^2 - 421.620 * (\text{TiO Index}) + 3902.4 \qquad (2a)$$

$$\text{M-Spec Type} = -1.0944 * (\text{TiO Index})^2 + 6.1537 * (\text{TiO Index}) - 1.3947 \qquad (2b)$$

Note that Equations 2a and 2b are slightly different than the original calibration (Equations A2 and A3) as given in the Appendix in Wasatonic *et al.* (2015); the current calibration was derived using updated atmospheric extinction and transformation coefficients and by re-combining some observed TiO-index calibration results as given in Tables 6 and 7 of the Appendix in Wasatonic *et al.* (2015). The effective temperatures were computed using the red supergiant spectral type/effective temperature scale from Table 5 of Levesque *et al.* (2005), and the M-spectral subtypes were obtained from Wing (1978) calibration stars. Further calibration details are given in section A1 of the Appendix in Wasatonic *et al.* (2015).
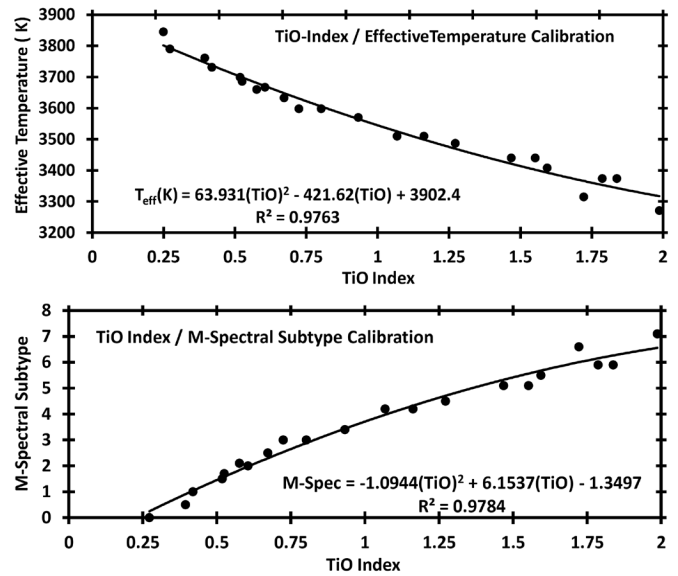

Figure 1. TiO/T_{eff} and TiO/M spectral sub-type calibrations used to compute changing Betelgeuse effective temperatures and M-spectral subtypes. Note that the determination coefficients (R^2) are both near 1.0, indicating high fit reliabilities.
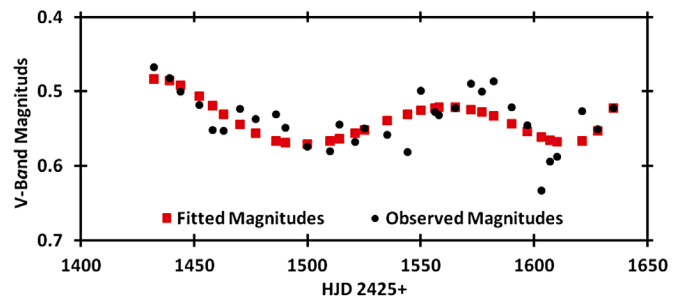

Figure 2. Example of fifth-degree polynomial fit (red squares) overlayed on actual V-band magnitudes (black dots) from the 1999/2000 observations.

For each of the four filters the raw photometer counts were reduced by FORTRAN programs that took into account conversions to Heliocentric Julian Day (HJD), atmospheric extinction, V-band color corrections, C-band $\lambda 1024$-nm color and mbol corrections, and UT, SSP-3 counts, and air mass interpolations. Using the reduced NIR magnitudes, TiO indicies, effective temperatures, luminosities, and radii were calculated.

All reduced magnitudes and calculated TiO indicies, effective temperatures, radii, and luminosities were then fitted with fifth-degree polynomials on a seasonal basis to generate smooth variations, and the fitted data were then used for final analyses. An example of fitted magnitudes overlayed on actual observations is given in Figure 2.

Betelgeuse was observed differentially over 981 nights in the NIR bands and 997 nights in the V-band from 1996 to 2021. The comparison star was HD 37160 (V = 4.09, B–V = 0.95, G9.5IIIb). Since the comparison star was considerably fainter than Betelgeuse, different SSP-3 amplifier gains had to be used during the observations, that is, when observing Betelgeuse itself the gain had to be reduced to avoid SSP-3 detector saturation. This gain difference was compensated for during the reduction process. Additionally, since the comparison star and Betelgeuse were separated by 4.14 degrees, atmospheric extinction effects

were minimized using photometric reduction techniques as described in Hall and Genet (1982) and Wing (1995). To insure the non-variability of the comparison star, the check star γ Orionis (HD 35468, V = 1.64, B–V = –0.22, B2 V) was observed differentially with respect to the comparison star on 389 nights in the V-band over the entire 25-year observational period. Discounting random observational noise, no variability > 0.025 magnitude was observed between these two stars.

To generate the NIR magnitudes of Betelgeuse itself, the NIR magnitudes of the comparison star itself had to be computed. In order to generate these magnitudes the comparison star was observed differentially with the check star, whose NIR magnitudes are given by Wing and Ridgway (1979). Over the course of the 25-year observational period, differential observations were conducted on 65, 66, and 69 separate nights using the A-band, B-band, and C-band filters, respectively, with the final calculated magnitudes being: A = 0.135 ± 0.002, B = 0.192 ± 0.003, and C = 0.689 ± 0.003.

The reduced magnitude of the C-band filter was used as an estimate of the apparent bolometric magnitude (mbol) as theorized by Wing (1992). This was done after transforming the reduced C-filter magnitude to an effective wavelength of λ1040 nm via a color term and applying a small magnitude adjustment. In using an adopted distance to Betelgeuse of 197 PC the absolute bolometric magnitude (M_{bol}), or intrinsic luminosity with respect to the sun ($L_\star / L_\odot$), could then be calculated. Details of C-filter magnitude corrections are given in section 2 of the Appendix in Wasatonic *et al.* (2015). Finally, knowing the calculated effective temperatures and intrinsic luminosities, radii were calculated from:

$$L = 4\pi\sigma(R)^2 (T_{eff})^4 \qquad (3)$$

where $\sigma = 5.67 \times 10^{-8}$ joule/s/m²/K⁴ (the Stefan-Boltzmann Constant).

3. Observations and analyses[1]

3.1. Magnitude variations and flux ratios

Figure 3 displays the 25-year V-band fitted magnitude variations in the upper panel and the calculated fitted TiO indices in the lower panel. The semiregular variability nature of Betelgeuse is apparent in examining the magnitude variations. That is, on a season-by-season basis, the magnitude fluctuations do not repeat in a consistent manner. The overall 25-year average V-band magnitude was V = +0.56 ± 0.03, which is near Dolan *et al.*'s (2016) adopted value of V = +0.51 as given in Table 1.

Note the inverse correlation between the V-band magnitude variations and the calculated TiO indices. This inverse correlation was expected, as the magnitude variations are due, in part, to molecular TiO dissociation that results in decreased absorption at λ719 nm, leading to V-band brightening. Subsequent molecular TiO formation results in increased absorption at λ719 nm, leading to V-band dimming. The TiO dissociation
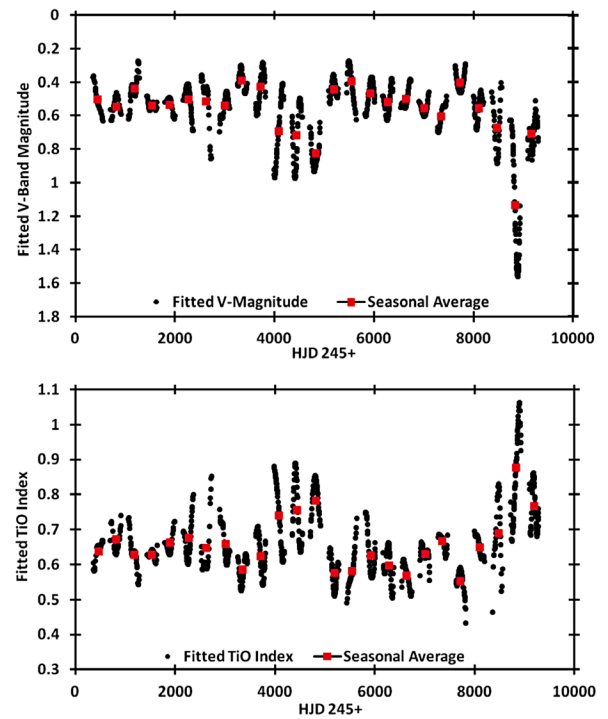

Figure 3. Upper panel: V-band magnitude variations; Lower panel: TiO index variations. Note the expected inverse correlation between these two quantities. The black dots represent the fitted magnitudes and TiO indices and the red squares represent seasonal averages.
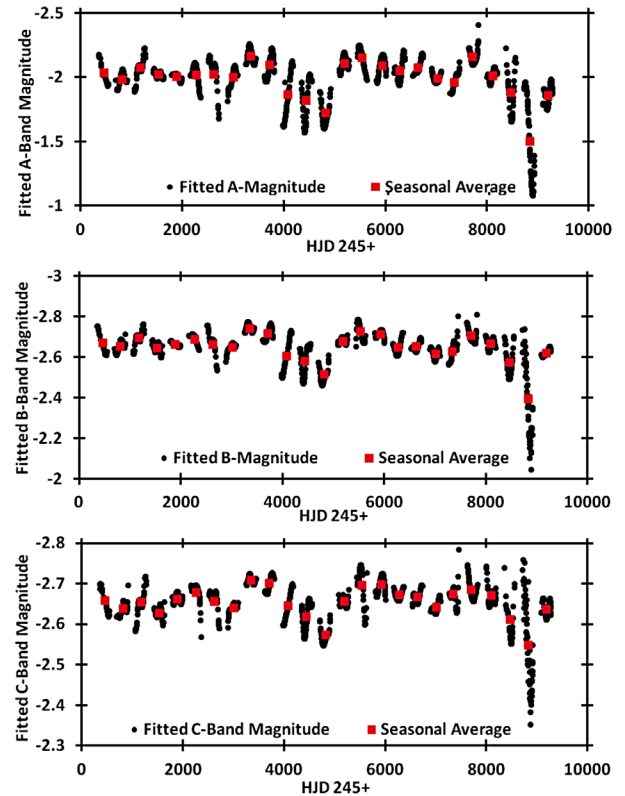

Figure 4. NIR magnitude variations; note the decreasing amplitudes between the A-band variations (~1.4 magnitudes) and the B- and C-band variations (~0.8 and ~0.4 magnitude, respectively). The black dots represent the individual fitted magnitudes, and the red squares represent seasonal averages.

---

[1] The full dataset is available through the AAVSO ftp site at ftp://ftp.aavso.org/public/datasets/3843-Wasatonic-502-alphaori.txt (if necessary, copy and paste link into the address bar of a web browser).

and formation events are themselves due to increasing and decreasing effective temperatures, respectively, which will be discussed in section 3.4 below.

Figure 4 displays the 25-year NIR magnitude variations. Note that the overall magnitudes are brighter with decreasing wavelength as progression is made from the λ719-nm A-band (upper panel) to the λ754-nm and λ1024-nm B- and C-bands (middle and lower panels). This effect was expected, as Betelgeuse radiates at a peak wavelength of λ793 nm, based on the 25-year overall average effective temperature of 3652 K. The peak wavelength was calculated using Wien's Law, which is:

$$\lambda_{max} = 2.898 \times 10^6 / T(K), \qquad (4)$$

where λ_{max} is expressed in nanometers. Additionally, it can be seen from the B- and C-band light curves that the magnitudes in these two bandpasses are nearly identical. Recall that from Table 2 the FWHM of the narrow-band B-filter is only 11 nm, while the FWHM of the intermediate-band C-filter is 42 nm, and that, as mentioned in section 2, after suitable conversions were done the C-filter magnitudes could be considered bolometric in nature. However, because of the similarities of the B- and C-band magnitudes, the B-band magnitudes may also be considered bolometric since the averaged 25-year flux ratio of the B- to the C-band magnitudes (f_b / f_c, as given in Equation 5b below) was 0.995. Therefore, the bolometric magnitude of Betelgeuse possibly can be measured at shorter wavelengths near λ754 nm than originally thought at λ1040 nm. This would mean that the total energy output of Betelgeuse can be measured from deeper atmospheric levels (at λ754 nm) rather than from the outer atmospheric energy levels of the entire star at λ1040 nm.

In Figure 3 note that during the GDE the V-band fitted minimum magnitude dropped to V = +1.56; comparing this minimum with its average V-band magnitude of +0.56 indicates the star appeared fainter by a factor of 2.5. However, in the C- (or bolometric) band (Figure 4) the star appeared fainter by a factor of only 1.355 (in comparing the GDE C-band minimum magnitude of –2.35 to the average C-band magnitude of –2.65). Thus during the GDE itself there was speculation that the star might soon become a supernova event due to its visual decrease in light by a factor of 2.5; however, this thought should have been tempered by the overall (bolometric) loss of only ~1.3 times its pre-GDE value, implying that the overall energy output dropped relatively little compared to the visual energy output, thereby rendering a supernova event as probably non-imminent.

NIR to V-band flux ratios were calculated using Equation 5a:

$$f_{ir} / f_v = 10^{-0.4 * (ir - v)} \qquad (5a),$$

where the quantity (ir − v) represents the difference in the seasonal magnitude averages (red squares in Figures 3 and 4) between the NIR bands and the V-band. Additionally, the flux ratios between the B-filter and C-filter seasonal average magnitudes were calculated from Equation 5b as given below:

$$f_b / f_c = 10^{-0.4 * (b - c)}, \qquad (5b)$$

where the quantity (b−c) is the difference between the B- and C-band average magnitudes in a given season. Over the course of the 25-year observational time frame, the average observed flux at λ719 nm was ~10.5 times the observed flux at λ550 nm (f_a / f_v = 10.494), and the averaged observed flux at λ754 nm and λ1024 nm was ~19.5 times the observed flux at λ550 nm (f_b / f_v = 19.308 and f_c / f_v = 19.562). These calculated ratios quantify the amounts of observed near-IR flux compared to the observed V-band flux. Additionally, it was seen that the f_b / f_c ratio remained fairly steady near unity over the 25-year observational time frame, implying bolometric magnitudes may be measured by either the narrow B-band filter or the intermediate C-band filter as discussed earlier.

It should be noted that during the GDE of 2019/2020 the NIR to V-band ratios were considerably higher than the above mentioned averages. Specifically, f_a / f_v was 11.35, f_b / f_v was 25.89, and f_c / f_v was 29.73; these higher flux ratios were due to the V-band flux at λ550 nm falling more steeply than the NIR fluxes, giving rise to the higher ratios, again indicative that what was observed was mainly a loss in visual light compared to loss of light in the NIR.

3.2. Amplitudes

While the Figure 3 and Figure 4 light curves themselves look quite similar, note that the amplitudes steadily decrease as progression is made from the V-band filter (upper panel, Figure 3) to the A-band filter (upper panel, Figure 4) to the B- and C-band filters (middle and lower panels, Figure 4).

The maximum total amplitudes over the entire 25-year time frame (excluding the GDE) are 0.701, 0.709, 0.311, and 0.212 magnitude in the V-, A-, B-, and C-bands, respectively. Table 3 lists the 25-year maximum and minimum magnitudes, the HJD of each occurrence for each filter, and the resulting total amplitude for each filter. It was a mild surprise that the A-band total amplitude was virtually identical to the V-band total amplitude. The A-band filter is specifically designed to measure the λ719-nm flux variations that are caused by TiO dissociations (less absorption) and formations (more absorption); to some extent these absorption variations could have affected the perceived flux through the wide-band V-filter, giving rise to near identical amplitudes. The central wavelengths of the B- and C-filters are located in relatively clear spectral regions and are thus not readily affected by changing TiO amounts, thus accounting for the lower overall total amplitudes.

The seasonal total amplitudes, however, are less than the overall 25-year total amplitudes in all four wavelength bands. Seasonal total amplitudes in each wavelength band were computed for those particular seasons with well defined local maxima and minima. The averaged seasonal total

Table 3. Amplitudes over 25 years.

Filter	Maximum	HJD (245+)	Minimum	HJD (245+)	Total Amplitude
V	0.274	5492	0.975	4412	0.701
A	−2.281	7817	−1.572	4409	0.709
B	−2.772	7633	−2.461	4781	0.311
C	−2.759	8729	−2.547	4781	0.212

amplitudes were 0.263 ± 0.041, 0.250 ± 0.041, 0.100 ± 0.016, and 0.061 ± 0.011 magnitude in the V-, A-, B-, and C-bands, respectively. It is important to realize, however, that seasonal total amplitudes are quite variable, but that a particular seasonal total amplitude will, as a rule, be less that any long-term observed total amplitude.

3.3. Periodicities

Despite the current SRc classification, both short- and long-term period searches using the V-band fitted magnitude variations were attempted by using the Data Compensated Discrete Fourier Transform (DCDFT) that is in the CLEANest routine of the Period Analysis Software (Peranso) package provided by Vanmunster (2021). To this end, the upper and lower panels of Figure 5 display the power spectra of the calculated V-band short- and long-term periods, respectively. The upper panel displays a dominant short-term period of 439 ± 5 days and a secondary period of 405 ± 4 days; these periods generally correspond with previously published results from Dupree *et al.* (1987), who reported a period of 420 days, and Karovska (1987), who reported a period (among five) of 383 days. The bottom panel displays a dominant period of 2209 ± 183 days and a secondary period of 4706 ± 884 days; the dominant period agrees somewhat with previously published results of Guinan (1984) and Goldberg (1984), who both report a period of 2109 days, and Stothers and Leung (1971), who reported a period of 2332 days. The long-term periods have larger uncertainties due to more probabilistic non-regular variations because of the longer time frame. It should be noted
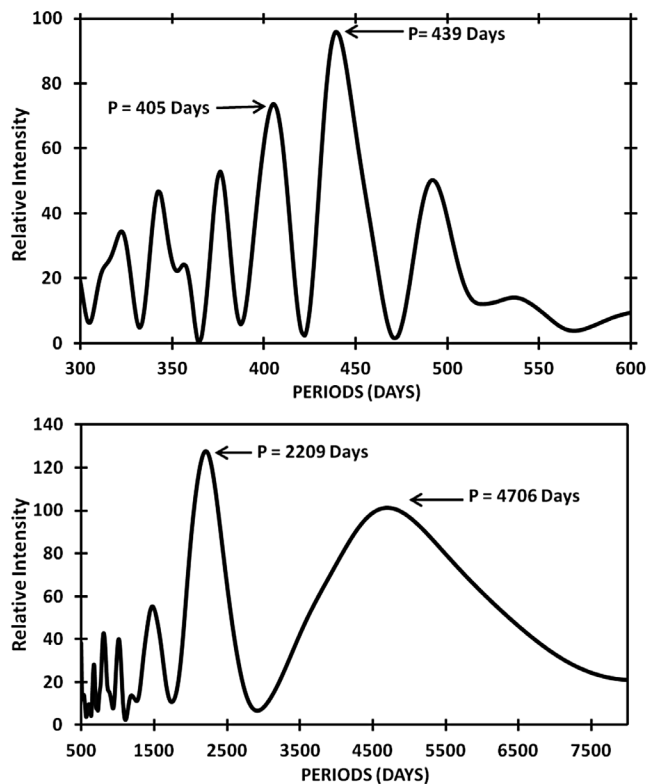
that these generated periods can be considered valid for only the 25-year observational time frame.

3.4. Radius, luminosity, and effective temperature variations

In addition to observing Betelgeuse for magnitude variations and periodicities, radius, luminosity, and effective temperature (hereinafter RLT) estimates were calculated using the NIR variable magnitudes. Effective temperatures were derived from using Equations 1 and 2a, luminosities were determined from the C-filter magnitudes after employing the needed conversions, and radii were the subsequently calculated via Equation 3. Figure 6 displays the RLT variations over the entire 25-year observational time frame; note that the radii and luminosities are given in terms of solar units. The fitted maximum effective temperature of 3731 K was calculated during 2016/2017 and the fitted minimum effective temperature of 3528 K was calculated during the Great Dimming Event of 2019/2020. Similarly the fitted calculated maximum and minimum luminosities were $114204\,L_\odot$ (2015/2016) and $70564\,L_\odot$ (2019/2020), respectively, and the fitted calculated maximum and minimum radii were $847\,R_\odot$ (2015/2016) and $710\,R_\odot$ (2019/2020), respectively.

From Figure 6 note that the effective temperature variations (lower panel) form positive correlations with both the V- and A-band magnitude variations (upper panels, Figures 3 and 4,

Figure 5. Short-tem (upper panel) and long-term (lower panel) Peranso-generated periods using the V-band fitted observations. The dominant (higher relative intensity) and secondary (lower relative intensity) periods are indicated in days.
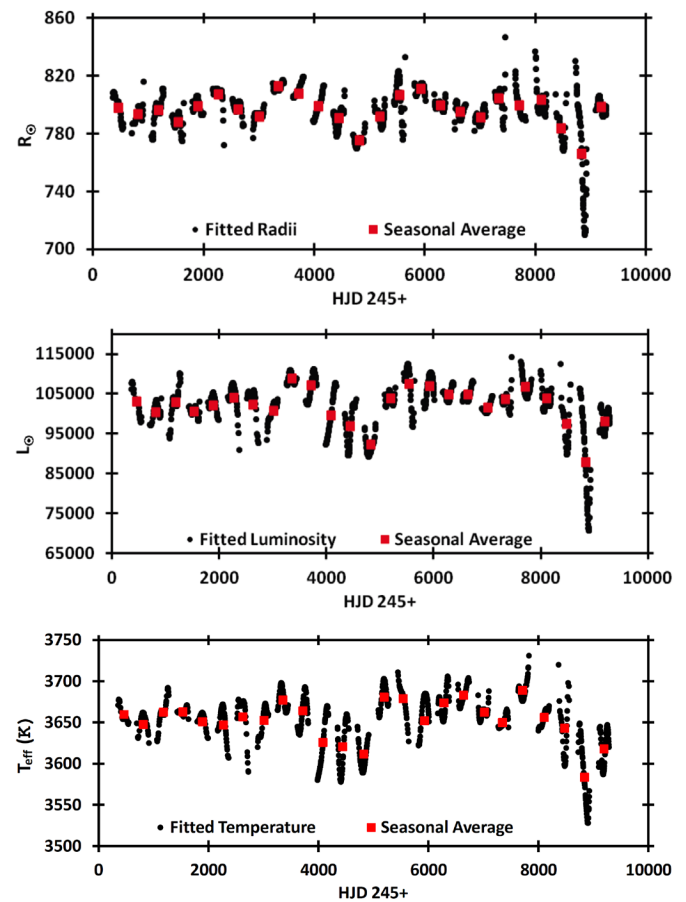

Figure 6. Calculated radius, luminosity, and effective temperature (RLT) variations. The radii and luminosities are given in solar terms. The black dots represent calculated fitted variations, and the red squares represent seasonal averages.

respectively) and form an inverse correlation with the TiO index variations (lower panel, Figure 3). These correlations (both direct and inverse) were expected, since increasing temperatures result in brighter magnitudes due to TiO molecular dissociation and hence less absorption at λ719 nm. Conversely, decreasing temperatures result in fainter magnitudes due to TiO re-formation and hence more absorption at λ719 nm. Despite reported asymmetries from an overall spherical shape of Betelgeuse (e.g. Gilliland and Dupree 1996), Equation 3 was used to calculate radii based on the effective temperature and luminosity observations, and hence the calculated radii should be viewed with caution. From Figure 7 it can be seen that the luminosity and radii variations form an overall positive correlation with respect to the temperature variations, although there is considerable scatter on a season-by-season basis. It is interesting to note that individual seasonal RLT variations at times show positive correlations, yet during other individual seasons the RLT inter-relationships show either negative correlations or no correlations at all. These anomalous RLT inter-relational discrepancies will be discussed in detail in subsequent papers which will also describe unusual relationships among the four-filter magnitude variations on a season-by-season basis. An example of a seasonal magnitude anomaly is given below in section 4.
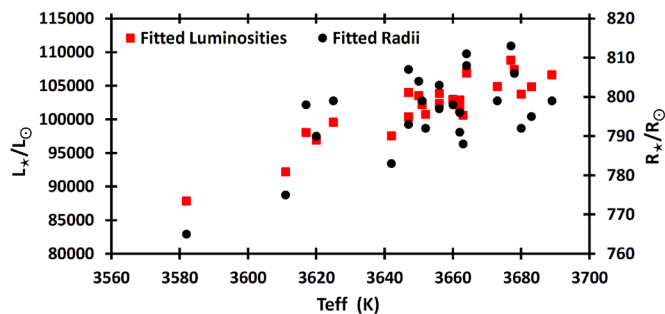

Figure 7. Net positive correlations of luminosity and radius with respect to effective temperature using seasonal averages that were depicted in Figure 6.
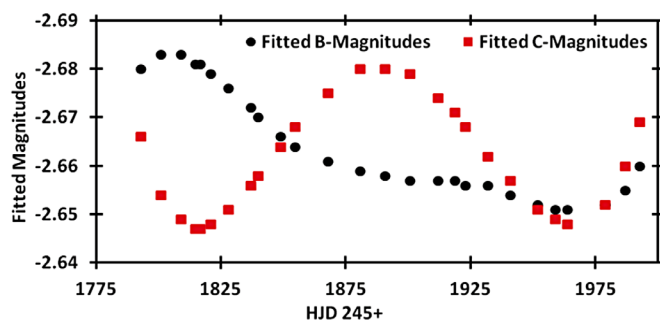

Figure 8. Season 5 (2000/2001) anomalous B-band (black dots) and C-band (red squares) relative magnitude variations. Note the C-band near-sinusoidal magnitude variation while the B-band magnitudes continually decrease throughout the season, contrary to expected uniform magnitude changes (both simultaneously increasing and/or decreasing).

4. Future research

It was stated in section 3.4 that, on a season-by-season basis, the interrelationships among effective temperatures, luminosities, and radii can at times show either a positive or negative correlation, or no correlations at all. Similar anomalies can also be seen in seasonal magnitude variations among the four observed bandwidths. An example of magnitude discrepancies is displayed in Figure 8, which displays the fitted B- and C-band magnitude variations from Season 5 (2000/2001). Note that while the C-band magnitudes (red squares) form an approximate sinusoidal curve, the B-band magnitudes (black dots) consistently decrease throughout most of the season. It is only near the end of the observing season that both the B-band and C-band magnitudes simultaneously increase. Thus, for most of the season these relative variations were unexpected, as both bands lie in relatively clear spectral regions and hence any radiative processes should be nearly identical, leading to approximately uniform magnitude variations. Future planned papers will examine in detail similar unexpected observations that have occurred in specific seasons which will reveal anomalies that are not apparent when examining the entire 25-year observational time frame in singly displayed light curves.

5. Summary

In examining the light curves (Figures 3 and 4) it is apparent that the SRc variable star classification is confirmed for Betelgeuse, as both the magnitude and amplitude variations are semiregular at best. Both V-band dominant long-term (2209 ± 183 days) and short-term (439 ± 5 days) periods were detected, providing astronomers the means to predict with some degree of certainty when the next local maximum or minimum should occur. However, due to the inherent semiregular nature of the star, any predicted times should be taken with caution. The NIR to V-band flux ratios indicate the observed flux from Betelgeuse is ~10 to ~20 times stronger in the NIR than the V-band, which was expected but now has been quantified. The overall 25-year averages of effective temperature at 3652 K, luminosity at ~$10^5 L_\odot$, and radius at 796 $R_\odot$ (based on an adopted distance of 197 PC) are consistent with current literature data. Subsequent papers will investigate in detail unusual four-filter magnitude variations with respect to each other and unusual RLT inter-relationships on a season-by-season basis. Finally, as evidenced by the GDE during the 2019/2020 observing season, continued observations are warranted to monitor the star for any unexpected and anomalous behavior.

6. Acknowledgements

References

Dolan, M. M., Mathews, G. J., Lam, D. D., Quynh Lan, N., Herczeg, G. J., and Dearborn, D. S. P. 2016, *Astrophys. J.*, **819**, 7.

Dupree, A. K., Baliunas, S. L., Guinan, E. F., Hartmann, L., Nassiopoulos, G. E., and Sonneborn, G. 1987, *Astrophys. J., Lett.*, **317**, L85.

Dupree, A. K., et.al. 2020, *Astrophys. J.*, **899**, 68.

Gilliland, R. L., and Dupree, A. K. 1996, *Astrophys. J., Lett.*, **463**, L29.

Goldberg, L. 1984, *Publ. Astron. Soc. Pacific*, **96**, 366.

Guinan, E. F. 1984, in *Cool Stars, Stellar Systems, and the Sun*, ed. S. L. Baliunas, L. Hartmann, Springer-Verlag, New York, 336.

Guinan, E. F., Wasatonic, R. J., and Calderwood, T. J. 2019a, *Astron. Telegram*, No. 13341, 1.

Guinan, E. F., Wasatonic, R. J., and Calderwood, T. J. 2019b, *Astron. Telegram*, No. 13365, 1.

Hall, D. S., and Genet, R. M. 1982, *Photoelectric Photometry of Variable Stars*, International Amateur-Professional Photoelectric Photometry (IAPPP), 13-2, 13-3.

Harper, G. M., Brown, A., and Guinan, E. F. 2008, *Astron. J.*, **135**, 1430.

Kaler, J. 2001, *Extreme Stars: At the Edge of Creation*, Cambridge University Press, New York, 125.

Karovska, M. 1987, in *Stellar Pulsations: A Memorial to John P. Cox*, eds. A. N. Cox, W. M. Sparks, S. G. Starrfield, Springer-Verlag, New York, 260.

Levesque, E. M., Massey, P., Olsen, K. A. G., Plez, B., Josselin, E., Maeder, A., and Meynet, G. 2005, *Astrophys. J.*, **628**, 973.

O'Gorman, E., Harper, G. M., Brown, A., Guinan, E. F., Richards, A. M. S., Vlemmings, W., and Wasatonic, R. 2015, *Astron. Astrophys.*, **580A**, 101.

Perrin, G., Ridgway, S. T., Coudé du Foresto, V., Mennesson, B., Traub, W. A., and Lacasse, M. G. 2004, *Astron. Astrophys.*, **418**, 675.

Petit, M. 1987, *Variable Stars*, Wiley, Chichester, NY, 71.

Stothers, R., and Leung, K. C. 1971, *Astron. Astrophys.*, **10**, 290.

Townes, C. H., Wishnow, E. H., Hale, D. D. S., and Walp, B. 2009, *Astrophys. J., Lett.*, **697**, L127.

Vanmunster, T. 2021, Peranso light curve and period analysis software, version 3.0.2.9 (http://www.peranso.com).

Wasatonic, R. P., Guinan, E. F., and Durbin, A. J. 2015, *Publ. Astron. Soc. Pacific*, **127**, 1010.

Wing, R. F. 1978, *Spectral Classifications and Color Temperatures for 280 Bright Stars in the Range K4–M8*, Ohio State University Press, Columbus, OH, 5–9.

Wing, R. F. 1992, *J. Amer. Assoc. Var. Star Obs.*, **21**, 42.

Wing, R. F. 1995, private communication.

Wing, R. F., and Ridgway, S. T. 1979, *Dudley Obs. Rep.*, No. 14, 253.